Integrating Finite Element Modelling and 3D Printing to Engineer Biomimetic Polymeric Scaffolds for Tissue Engineering

Rossana Schipani[a,b], David R. Nolan[a,b], Caitríona Lally[a,b] and Daniel J. Kelly[a,b,c,d]*

[a]*Trinity Centre for Bioengineering, Trinity Biomedical Sciences Institute, Trinity College Dublin, Dublin, Ireland;*

[b]*Department of Mechanical and Manufacturing Engineering, School of Engineering, Trinity College Dublin, Dublin, Ireland;*

[c]*Department of Anatomy, Royal College of Surgeons in Ireland, Dublin, Ireland;*

[d]*Advanced Materials and Bioengineering Research Centre (AMBER), Royal College of Surgeons in Ireland and Trinity College Dublin, Dublin, Ireland.*

**Corresponding Author: Tel: +353-1-8963947, email: kellyd9@tcd.ie*

Abstract

The suitability of a scaffold for tissue engineering is determined by a number of interrelated factors. The biomaterial should be biocompatible and cell instructive, with a porosity and pore interconnectivity that facilitates cellular migration and the transport of nutrients and waste products into and out of the scaffolds. For the engineering of load bearing tissues, the scaffold may also be required to possess specific mechanical properties and/or ensure the transfer of mechanical stimuli to cells to direct their differentiation. Achieving these design goals is challenging, but could potentially be realised by integrating computational tools such as finite element (FE) modelling with three-dimensional (3D) printing techniques to assess how scaffold architecture and material properties influence the performance of the implant. In this study we first use Fused Deposition Modelling (FDM) to modulate the architecture of polycaprolactone (PCL) scaffolds, exploring the influence of varying fibre diameter, spacing and laydown pattern on the structural and mechanical properties of such scaffolds. We next demonstrate that a simple FE modelling strategy, which captures key aspects of the printed scaffold's actual geometry and material behaviour, can be used to accurately model the mechanical characteristics of such scaffolds. We then show the utility of this strategy by using FE modelling to help design 3D printed scaffolds with mechanical properties mimicking that of articular cartilage. In conclusion, this study demonstrates that a relatively simple FE modelling approach can be used to inform the design of 3D printed scaffolds to ensure their bulk mechanical properties mimic specific target tissues.

Keywords: Three-dimensional Printing, Scaffold Design, Finite Element Modelling, Mechanical Properties, Tissue Engineering

1 Introduction

Tissue engineering applications often require the use of porous and biocompatible three-dimensional (3D) scaffolds that serve as temporary templates for cell attachment and proliferation, ultimately promoting tissue specific extracellular-matrix secretion and functional regeneration [1,2]. For the engineering of many tissues, the geometry and mechanical properties of the scaffold are key factors that must be carefully tuned to appropriately direct regeneration. Geometrically, the scaffold needs both a suitable external architecture to properly fit the defect, and an internal architecture with sufficient porosity to facilitate cell migration and cell-cell interactions. Mechanically, it should have sufficient strength to resist physiological loading while appropriately distributing such stresses to the surrounding tissue during the regeneration process [3].

3D printing technology in tissue engineering allows the fabrication of patient-specific scaffolds with high cell ingrowth capability, appropriate pore interconnectivity, highly controlled internal geometry and more recently the incorporation of bioinks containing cells [4–6]. Among the number of 3D printing techniques available, Fused Deposition Modelling (FDM) has shown great potential in advancing the development of functional tissue replacements, as it enables the fabrication of scaffolds with precisely defined compositions and architecture [7,8]. Highly interconnected pore geometries with a wide range of pores size can be obtained by varying printing parameters such as needle diameter, extrusion pressure and speed [7–9]. Moreover, mechanically robust scaffolds can be produced with mechanical behavior mimicking that of several biological tissues [9–11].

From a mechanical point of view, there is still a lack of knowledge on the behavior of 3D printed structures under compressive load and how such implants might respond to physiological loading conditions. The absence of a simple and efficient framework to explain the micromechanical behavior of 3D scaffold structures can limit or slow down

the development of appropriate tissue engineered scaffold designs. Previous studies attempting to develop functional scaffold designs have typically adopted a "trial-and-error" approach, where modifications to an existing design are assessed using experimental work. Computational methods that simulate the mechanical behavior of 3D constructs can also provide valuable insights into the structure-function relations of such implants [6,12]. A number of studies have used Finite Element Analysis (FEA) to optimize and/or evaluate scaffold designs in terms of oxygen diffusion [13,14], mechanical properties [15,16] and cell response to external stimuli [13,17]. The accuracy of such FE models strongly depends on how precisely the architecture of the printed structure is represented. Discrepancies between the originally designed structure and the actual printed geometry will always occur during the FDM process. For example, filaments from one layer of a printed scaffold fuse to differing degrees into the previous layer, altering the geometry of the scaffold. The importance of considering these geometrical differences when developing FE models of 3D printed structures has only recently been appreciated [21,22]. Therefore, FE analysis aided design of 3D printed scaffolds must consider the actual printed geometry of the construct, ideally without resorting to use of computationally expensive techniques that would limit the widespread use of such approaches.

The overall goal of this study was to develop a computationally efficient and accessible FE modelling strategy that could be used to design 3D printed polycaprolactone (PCL) scaffolds with user-defined mechanical properties. To this end, we first printed a range of PCL scaffolds with altered fibre spacing and fibre diameters, and then created Computer Aided Design (CAD)-based FE models of both the idealized scaffold designs (pre-fabrication) and the actual printed scaffolds (post-fabrication). The advantage of modelling actual printed geometries and the ability of such models to predict the mechanical behavior of complex 3D structures is demonstrated by comparing

computational predictions to experimental measurements. The utility of this integrated approach is demonstrated by designing and 3D printing scaffolds with defined stiffness and elasticity, with a particular focus on articular cartilage tissue engineering. Computational efficiency will be ensured by using CAD-based scaffold representations, that only account for key geometrical features of the actual printed geometry parameters (e.g. fibre diameter, fibre spacing, layer fusion), to predict the mechanical behavior of 3D printed scaffolds. Using CAD-based FEA in this way is advantageous as there is no need to develop sample-specific models that require expensive and time-consuming imaging techniques (i.e. micro-computed tomography (micro-CT) to determine the geometry of the scaffolds.

2 Materials and methods

2.1 Scaffold design and fabrication

All scaffold geometries were designed to obtain cube shaped constructs with dimensions 9 mm x 9 mm x 4 mm. To investigate how geometry features can influence scaffold mechanical properties and porosity, five different architectures were obtained by varying fibre spacing (s) (1 or 1.5 mm), fibre diameter (d) using two different needle sizes (25 or 30 Gauge) and internal fibre pattern (*Aligned*, *Single Offset* or *Double Offset*). Scaffold geometrical features are described in Figure 1a-d. The *Aligned* architectures (Figure 1b) were characterized by layer X plotted orthogonally to layer X-1 (resulting in a 90° angle) and was plotted in the same relative position of layer X-2. The *Single Offset* (Figure 1c) and *Double Offset* (Figure 1d) patterns are also orthogonal architectures characterized by layer X being printed with an offset distance, which is half the fibre spacing, relatively to the position of layer X-2. Offset layers are present only in the xz-plane for *Single Offset*

structures (showed in red in Figure 1c), whereas they are present in both xz- and yz-planes for *Double Offset* geometries (showed in red in Figure 1d). Fibres orientation was modified after the deposition of two consecutive layers in all geometries to provide the scaffolds with high side porosity. All constructs were manufactured using the 3D Discovery bioplotter purchased from RegenHU (Switzerland) with spatial resolution of ± 5 µm. PCL pellets with an average molecular weight (Mn) of approximately 50,000 Da (CAPA 6500D, Perstorp, Sweden) were used as received. Porous PCL frames were fabricated via FDM using the parameters reported in Table 1.

2.2 Scaffold characterization

2.2.1 Geometry analysis

The geometry of the PCL scaffolds post-printing was characterized using micro-CT. Scans were performed using a Scanco Medical 40 µCT system (Scanco Medical, Switzerland) with a 70 kV and 114 µA x-ray source with a voxel size of 16 µm. Simpleware™ ScanIP (Synopsys,Inc., USA) was used for processing, segmentation, 3D model reconstruction and analysis of the previously obtained CT images. Scaffolds fibre diameter and inter-spacing (inter-s) were measured from the top cross-sectional view of the reconstructed model, while the length of two consecutive fused layers was determined from the front cross-sectional view. Layer Fusion was calculated as follows:

$$Layer\ Fusion\ (mm) = (2 * designed\ LT) - FL \quad (1)$$

where LT refers to the ideally designed Layer Thickness (Figure 1) and FL indicates the length of two consecutive Fused Layers in the fabricated constructs.

2.2.2 Porosity

The theoretical porosity (P_t) of the designed scaffolds was estimated by volumes as follows:

$$P_t\ (\%) = 1 - \frac{V_{scaffold}}{V_{solid}} * 100 \quad (2)$$

where $V_{scaffold}$ is the theoretical volume of the porous cubic scaffold and V_{solid} is the volume of a non-porous cube with the same scaffold dimensions.

The porosity of the 3D printed structures was evaluated experimentally using the gravimetric method according to the following equation:

$$P_e\ (\%) = 1 - \frac{\rho_{scaffold}}{\rho_{PCL}} * 100 \quad (3)$$

where P_e is experimental porosity, $\rho_{scaffold}$ is the apparent density of the scaffold, whereas ρ_{PCL} is the PCL density which is 1.145 g/mL. $\rho_{scaffold}$ was obtained as:

$$\rho_{scaffold}(g/mL) = \frac{m_{scaffold}}{V_{scaffold}} \quad (4)$$

where $m_{scaffold}$ and $V_{scaffold}$ are the weight and the volume of the scaffold respectively. The weight of the 3D printed constructs was quantified using an analytical balance (Mettler Toledo Excellence XS205 DualRange with sensitivity of 0.01 mg).

2.3 Mechanical characterization

Mechanical tests were carried out in unconfined compression in air at room temperature (~25°C) using a twin column Zwick universal testing machine (Zwick, Roell, Germany). All samples (n = 4 per group) were subjected to a compressive-strain cycle load up to 5 cycles with nominal strain amplitude of 10, 20, 30, 40 and 50 % in sequence. The specimens were compressed at a cross-head speed of 1mm/min between two impermeable metal platens after applying an initial preload of 1 N. A 2,500 N load cell was used for

testing samples produced with a 25 Gauge needle, whereas a 100 N load cell was used for those fabricated with a 30 Gauge needle. The load versus displacement data were recorded throughout. The engineering stress and strain were calculated by dividing the load value with the initial apparent cross-sectional area of each sample and the displacement value with the initial sample height, respectively. The elastic modulus was taken as the slope of the initial linear region of the plotted stress-strain curve obtained from the first compressive cycle.

The scaffold permanent deformation (PD), defined as apparent uniaxial plastic strain in the material, was calculated at the end of the tests as follows:

$$PD\ (\%) = \frac{Test\ Speed * \Delta t_5}{h_0} * 100 \quad (5)$$

where Δt_5 (s) is the interval of time at the start of the 5th cycle in which no force is applied, assuming the sample underwent permanent deformation, while h_0 (mm) is the height of the sample prior to test.

2.4 Finite element analysis

To predict the compressive properties of the 3D printed scaffolds, CAD-based FE models were developed using ABAQUS v6.14 (DS Simulia, USA). For *Aligned 1* (*d*=0.3mm; *s*=1.0mm) and *Aligned 2* (*d*=0.3mm; *s*=1.5mm) structures, ramp compression tests until 10 % strain were simulated for both an idealized and an actual printed scaffold representation. In the idealized models, pre-fabrication scaffold geometry features were reproduced. On the other hand, actual printed scaffold models were characterized by geometry parameters measured post-fabrication including layer fusion. For *Aligned 3* (*d*=0.12mm; *s*=1.5mm), *Single Offset* (*d*=0.12mm; *s*=1.5mm) and *Double Offset* (*d*=0.12mm; *s*=1.5mm) structures, only actual printed models were developed simulating

183 the same mechanical loading conditions as for *Aligned 1* and *Aligned 2*. Both idealized
184 and actual printed models consisted of a symmetric structure of approximately cubic
185 scaffolds (4.5 mm x 4.5 mm x 4 mm). For all groups, the nodes at the top face of the
186 scaffolds were given a displacement of approximately 0.4 mm corresponding to 10 %
187 compressive strain. The nodes at the bottom ends of the constructs were constrained only
188 in the direction of loading, allowing for scaffold expansion in the remaining two
189 directions due to the Poisson's effect. Symmetry boundary conditions were also applied
190 as the model was reduced to a quarter section cut along the xz and yz planes of symmetry.
191 Therefore, x and y DOFs perpendicular to the symmetry planes were constrained.

192 The effective compressive modulus of the constructs was determined from the stress and
193 strain values of the linear region of the curve calculated from the displacement and
194 resultant reaction force data computed from the simulations. To compare the predictions
195 to the experiments, the resultant reaction force was multiplied by four to evaluate the
196 models outputs for the entire constructs. Isotropic elastic behaviour was initially assumed
197 for *Aligned 1* and *Aligned 2* models. Quadratic ten-node tetrahedral elements (C3D10)
198 were used. Table 3 summarizes the material properties of PCL which were obtained from
199 literature [19,23,24].

200 *2.4.1 Elastoplastic material model*

201 As PCL will deform plastically once the stress in the material exceeds its yield stress, an
202 elastoplastic material model is preferable to an elastic material model when the stress in
203 the material is expected to exceed the yield stress during loading [25,26]. To predict more
204 accurately the PCL scaffolds' stress-strain behaviour under compression, uniaxial
205 elastoplastic models were implemented (only for the actual printed geometries for all
206 scaffold groups). The same model configuration and boundary conditions as in the purely

elastic material models were applied. The plasticity model used was the von Mises yield criterion with isotropic hardening. To define the stress-strain curve, the yield and failure points of the material were considered as found in literature [23]. The implemented material parameters are summarized in Table 3. In Abaqus the plastic input parameters required were true stress and true plastic strain. Assuming no volume change in the specimen, the true stress (σ_{true}) was calculated as follows:

$$\sigma_{true} = \sigma_{eng} * (1 + \varepsilon_{eng}) \quad (6)$$

where σ_{eng} and ε_{eng} are engineering stress and strain.

The true total strain (ε_{true}) was calculated as:

$$\varepsilon_{true} = ln(1 + \varepsilon_{eng}) \quad (7)$$

from which the true plastic strain (ε_{pl}) was obtained as:

$$\varepsilon_{pl} = \varepsilon_{true} - \varepsilon_{el} = \varepsilon_{true} - \left(\frac{\sigma^{y}_{true}}{E}\right) \quad (8)$$

where ε_{el} is the elastic strain, σ^{y}_{true} is the true yield stress and E is the Young's modulus.

2.4.2 Determination of permanently deformed element volume fraction

To determine theoretically which scaffold architecture was more likely to undergo higher permanent deformation, the element volume fraction experiencing stress greater than 17 MPa, which is approximately the yield stress of PCL [23,24], was quantified as follows:

$$Element\ Volume\ Fraction\ (\%) = \frac{(element\ volume_{\sigma>17MPa})}{(total\ element\ volume)} * 100 \quad (9)$$

where element volume$_{\sigma>17MPa}$ represents the volume of the elements in the FE model showing stress greater than 17 MPa, whereas total element volume represents the volume of all the elements composing the scaffold model.

2.5 Statistical Analysis

Statistical analysis was performed using GraphPad (GraphPad Software, La Jolla California USA). Compressive modulus, porosity and permanent deformation analysis for varying filament spacing (*Aligned 1* vs. *Aligned 2*) and filament diameter (*Aligned 2* vs. *Aligned 3*) were examined using a student's t-test where means were compared. One-way analysis of variance (ANOVA) with the addition of Tukey's correction was used for multiple comparisons testing (*Aligned 3* vs. *Single Offset* vs. *Double Offset*). Results are expressed as mean ± standard deviation. For all comparisons, the level of significance was $p \leq 0.05$.

3 Results

3.1 The effect of filament diameter and spacing on the porosity and mechanical properties of 3D printed PCL scaffolds

Scaffold design and fabrication

To evaluate the effect of filament diameter and spacing on both the porosity and mechanical properties of 3D printed PCL scaffolds, three different idealized architectures were designed as shown in Figure 1b. The designed constructs were characterized by a fibrous network comprising of aligned filaments stacked in horizontal layers that followed a 0°0° - 90°90° pattern. *Aligned 1* and *Aligned 2* have a filament diameter of 0.26 mm (25 gauge needle) and two different spacings, 1 and 1.5 mm respectively. This resulted in filament inter-spacings of 0.74 mm for *Aligned 1* and 1.24 mm for *Aligned 2*.

To study the effect of filament diameter, *Aligned 3* architecture had a fibre diameter of 0.16 mm (30 gauge needle), while the fibre spacing was the same as the *Aligned 2* design (1.5 mm), resulting in a fibre inter-spacing of 1.34 mm.

The actual printed structures of the different scaffold designs are shown in Figure 2. 3D printing allowed for accurate and controlled deposition of PCL filaments, although micro-CT reconstructions demonstrate that some fibre diameter inhomogeneities exist in all three structures (Figure 2a-c). From the CT scans, the average fibre diameter was found to be approximately 0.3 mm in both the *Aligned 1* and *Aligned 2* architectures, whereas the filament diameter was about 0.12 mm for *Aligned 3*. Therefore, the inter-spacing between consecutive struts was smaller in *Aligned 1* (0.660 ± 0.017 mm) and *Aligned 2* (1.168 ± 0.089 mm) compared to the ideal designs, while it was bigger in *Aligned 3* (1.373 ± 0.025 mm). This had an effect on the resultant porosity of the actual printed scaffolds (Table 2). Compared to the idealized structures, *Aligned 1* and *Aligned 2* structures were less porous, whereas *Aligned 3* scaffolds had greater porosity. From the cross-sections of the CT scan images (Figure 2), it was observed that the printed filaments in all architectures did not have a regular rounded shape as ideally designed. This is because some degree of fusion between consecutively deposited layers occurred. Layer Fusion, which is considered 0 in the ideal designs, was quantified according to equation (1). It was found to be approximately 0.08 mm in *Aligned 1* and *Aligned 2*, whereas it was approximately 0.02 mm in *Aligned 3* (Table 2).

Constructs porosity, permanent deformation and mechanical properties

The compressive modulus and the extent of permanent deformation following the application of cyclic strain was calculated for each scaffold design (Figure 3a). Representative stress-strain plots of the first loading cycle for the three architectures are

shown in Figure 3b. As expected, increasing the filament fibre spacing from 1 mm (*Aligned 1*) to 1.5 mm (*Aligned 2*) increased the porosity and reduced the compressive modulus of the resulting scaffold (Table 2; Figure 3c). Both *Aligned 1* and *Aligned 2* geometries experienced permanent deformation after the application of the first compressive cycle (10 % applied strain) as it is shown in Supplementary Figure 1a,b for *Aligned 1* and *Aligned 2* scaffolds, respectively. Overall, the higher porosity scaffolds (*Aligned 2*) underwent higher permanent deformation (~25 %) compared to the less porous constructs (*Aligned 1*; ~22 %) (Figure e). Reducing the filament diameter (*Aligned 3*) also increased the porosity and reduced the compressive modulus of the scaffold (Table 2; Figure 3d). Moreover, lower permanent deformation was observed (Figure 3f).

3.2 FE models incorporating actual printed geometries can accurately predict the mechanical behaviour of 3D printed scaffolds

FE simulations of unconfined ramp compression tests were first performed using both idealized and actual printed geometries for the *Aligned 1* (Figure 4a,c) and *Aligned 2* (Figure 4b,d) structures using an elastic material model. In idealized *in silico* models, the ideally designed geometry parameters generated by CAD models were used to represent the constructs. In actual printed models, scaffolds were reproduced using the structural features measured post-fabrication where the actual fibre diameter and the amount of fusion between layers was included as model parameters. The von Mises stress was predicted to be higher at the crossover areas between consecutive printed layers for both idealized (Figure 4a,b) and actual printed (Figure 4c,d) model for the *Aligned 1* (Figure 4a,c) and *Aligned 2* (Figure 4b,d) scaffolds. Comparing the predicted stress-strain behaviour with the experimental results (Figure 5a,c), it can be observed that using the idealized representation of both *Aligned 1* (Figure 5a) and *Aligned 2* (Figure 5c) scaffolds

297 resulted into a significant underestimation of the bulk compressive modulus (Figure
298 5b,d). On the other hand, the actual printed models, which reproduced key scaffold
299 geometrical features (including layer fusion) as they were measured after fabrication,
300 showed good agreement with the experimental measurement of compressive modulus for
301 the *Aligned 1* (Figure 5b) and *Aligned 2* (Figure 5d) scaffolds. Nevertheless, actual printed
302 models that considered only elastic material properties failed to accurately predict the
303 stress-strain response, specifically the apparent transition from the linear elastic to the
304 plastic region under compression (Figure 5a,c).
305 Due to the architecture of these scaffolds it is expected that some local permanent
306 deformation will occur within the body of the scaffold once the localized stress exceeded
307 the material yield stress (the yield stress of PCL is estimated to be ~17 MPa [23,24]).
308 Therefore, an elastoplastic material model for PCL was introduced and simulations of
309 ramp compression tests were performed only for the actual printed configurations of both
310 *Aligned 1* (Figure 4e) and *Aligned 2* (Figure 4f). The predicted peak values of von Mises
311 stress were lower using the elastoplastic material model (Figure 5a,c). Furthermore, the
312 predicted stress-strain behaviour was more representative of experimental observations.
313 To evaluate the effect of varying filament diameter on scaffold mechanical
314 properties using FEA, *in silico* models of the *Aligned 3* constructs were also developed
315 using an elastoplastic material model and the actual printed geometry (Figure 6d-f). When
316 comparing *Aligned 2* and *Aligned 3* models, it can be observed once again that the
317 compressive forces are mainly supported at the filament junctions of adjacent layers,
318 although the stresses generated within the *Aligned 3* structure were lower compared to
319 *Aligned 2* (Figure 6a,d). The actual printed elastoplastic models were again capable of
320 accurately predicting the stress-strain behaviour (Figure 6e) and compressive modulus
321 (Figure 6f) of the scaffolds.

3.3 FE modelling to inform the design of 3D printed scaffolds with user defined mechanical properties

Having developed a computational framework that was able to accurately predict the uniaxial compression behaviour of 3D printed scaffolds, we next sought to leverage this approach to design scaffolds with biomimetic mechanical properties. Articular cartilage has a region specific-compressive modulus that varies from approximately 0.25 MPa to 1.8 MPa [27,28]. Ideally scaffolds designed to regenerate this tissue should have mechanical properties falling in the aforementioned range to provide a physiological-like mechanical environment.

The effect of varying filament pattern of fibrous constructs was evaluated. Figure 1c,d shows the strategies adopted to modify the scaffold fibre arrangement starting from the *Aligned 3* structure. The new designed architectures had the same filament diameter and spacing as *Aligned 3*, but different filament pattern. The *Single Offset* architecture (Figure 1c) was characterized by offset layers present only in the xz-plane, whereas it showed a regular orthogonal arrangement in the yz-plane. The *Double Offset* scaffold (Figure 1d) differed from the previous one because it had offset layers in both xz- and yz-planes. The offset was set to 0.75 mm (half the fibre spacing) in both cases. *Single Offset* and *Double Offset* mechanical properties were predicted simulating compression tests as done previously. Von Mises stress plots for the *Single Offset* architecture (Figure 7a) were similar to the previously analysed structures if looking at the yz-plane where filaments are arranged orthogonally with no offset. Here higher levels of stress were experienced at the points where filaments crossed over. On the xz-plane, the stress was not particularly concentrated in certain areas, but it was more homogeneously distributed through the

346 fibres.

347 In the *Double Offset* architecture model (Figure 7b), the same homogeneous stress
348 contour, which was present only in the xz-plane for the *Single Offset* model, was observed
349 throughout. This resulted in overall lower levels of stress experienced by the *Double*
350 *Offset* architecture. Predicted compressive stress-strain curves (Figure 7c) showed that
351 varying the filament pattern of the porous scaffolds from *Aligned 3* to *Single Offset* and
352 *Double Offset* decreased the stiffness of the constructs. This was confirmed when
353 calculating the compressive modulus (Figure 7d) which was 1.88, 0.56 and 0.22 MPa for
354 *Aligned 3*, *Single Offset* and *Double Offset* respectively.

355 To predict which architecture is more likely to undergo higher permanent deformation,
356 the element volume fraction of each model which experienced stress greater than 17 MPa
357 (PCL yield stress) was calculated according to equation (9). Figure 7e shows the
358 quantified element volume fraction for the three analysed models. It was predicted that
359 the *Aligned 3* configuration had the highest volume fraction (9.56 %) indicating this was
360 the structure that would experience more permanent deformation when subjected to 10 %
361 compression. The *Single Offset* model had a volume fraction of 4.44 % and the *Double*
362 *Offset* model had 0.2%, thereby the latter having the lowest plastic deformation.

363 *3.3.1 Models validation*

364 *Single Offset* and *Double Offset* PCL constructs were 3D printed according to the
365 fabrication parameters used for the *Aligned 3* architecture as reported in Table 1. Figure
366 8a shows microscope images of the obtained scaffolds. Constructs were mechanically
367 tested following the same cyclic compression test protocol applied for the previous
368 experiments. Representative stress-strain curves of the first loading cycle are shown in
369 Figure 8b, in which *Aligned 3*, *Single Offset* and *Double Offset* mechanical properties are

compared. As was predicted, *Double Offset* constructs are the softest whereas *Aligned 3* structures are the stiffest among the three groups. This was evidenced by the differences in slope of the stress-strain curves. Moreover, the trend of the experimental curves matched the predicted ones. The fabricated scaffolds where characterized by high porosity which was about 90 % regardless of the filament pattern chosen (Figure 8c,d). In good agreement with the computational results, the *Single Offset* and *Double Offset* constructs had a compressive modulus of 0.817 ± 0.02 MPa and 0.320 ± 0.03 MPa respectively (Figure 8c). Furthermore, varying the arrangement of the scaffold filaments reduced the permanent deformation the constructs underwent after being subjected to cyclic compressive loadings. All scaffold geometries underwent plastic deformation after being subjected to 10 % compressive strain (Supplementary Figure 1c-e). Permanent deformation at the end of the test was measured to decrease from about 18 % in *Aligned 3* structures to approximately 16 and 14 % in *Single Offset* and *Double Offset* constructs respectively (Figure 8d). Once again, CAD-FE models based on actual printed scaffold geometry proved to be an efficient approach to design constructs with desired structural and mechanical properties.

4 Discussion

The fabrication of scaffolds with a controlled shape and interconnected pore network, as well as appropriate mechanical properties, is fundamental when developing tissue engineered constructs [1,2,10,29,30]. 3D printing allows such control and permits the creation of constructs that serve as temporary templates while the extracellular matrix is produced, and can provide a mechanical environment conductive to tissue formation, especially when combined with soft hydrogel materials [31–35]. Computational modelling has been

increasingly applied to tissue engineering in order to aid in the design of such 3D scaffolds [36–39]. However, it can be challenging to develop FE models capable of accurately predicting scaffolds mechanical properties, at least in part due to unintended geometrical differences between the idealized and actual fabricated scaffolds [3,40,41]. Herein we described a strategy for designing 3D printed scaffolds with different structural and mechanical properties that is informed by a FE model that accounts for differences between the idealized scaffold geometry and what is eventually printed. Models of different scaffold architectures provided an insight into the structure-function relation of such scaffolds, and how modifying specific structural features can tailor the mechanical properties to those of a wide range of native tissues.

Using FDM, we produced a number of scaffolds made of PCL, which is a synthetic polymer widely used in 3D printing due to its biocompatibility, low melting temperature and mechanical stability [9,31,42,43]. The optimal sets of fabrication parameters for two different needle sizes (25 and 30 Gauge) were chosen to obtain defined porous structures with a good resolution and to avoid delamination between consecutively printed layers. Varying PCL scaffold geometrical features such as filament spacing and diameter had an effect on scaffold porosity, mechanical properties and plastic deformation. Increasing the fibre spacing from 1 mm (*Aligned 1*) to 1.5 mm (*Aligned 2*), but maintaining the same fibre diameter, resulted in structures with a higher porosity and therefore a lower compressive modulus. The more porous scaffolds also experienced higher permanent deformation. This may be due to sagging of the filaments when spanning from one fibre to the next, resulting in densification (impacting of the fibres against one another) of the scaffold occurring earlier when compression forces are applied. Scaffold stiffness further decreased whereas porosity increased when reducing fibre diameter (*Aligned 3*), although lower permeant deformation was observed. This is likely due to the lower stresses (and

hence material yielding) that are predicted to be generated within the scaffolds with lower fibre diameters as they are compressed.

Using micro-CT, we revealed geometric discrepancies between idealized and actual printed structures which are dependent on the fabrication process. Depending on the set of fabrication parameters used, the PCL filament diameter was either larger (for the 25 Gauge needle) or smaller (for the 30 Gauge needle) than originally designed. Moreover, the shape of the individual fibres was hard to distinguish as consecutively printed layers fused together post-extrusion. Such discrepancies impact both scaffold geometry and mechanical properties [8,44,45], but to date there are only few modelling techniques that have simulated these geometrical variations which have mainly focused on scaffolds for the regeneration of hard tissues [21,22,46–49]. For example, Campoli et al. [47] utilized FE models that implemented variations in the cross-section area of the struts in porous metallic biomaterials, showing good predictions when comparing computational and experimental results. Melancon et al. [48] developed a morphological map that would capture structural differences post-fabrication of porous biomaterials, which was then used to create statistical based numerical models that incorporated such geometrical irregularities. These models produced more reliable predictions of experimentally measured mechanical properties. Ravari et al. [49] developed a strategy to take account of variations in filament diameter into their FE models of 3D printed structures, which also improved the predictive capacity of the computational models. Naghieh et al. [22,46] investigated the effect of fusion between the different layers in 3D printed scaffolds, and again demonstrated the importance of considering this when developing accurate FE models. In the current study, a FE modelling framework was used to design scaffolds with mechanical properties suitable for soft tissue applications. CAD-based FE models of the idealized and actual printed scaffold architectures were developed to study the impact of such geometrical

differences when predicting the scaffold mechanical properties. Our models demonstrated that including layer fusion is essential to accurately modelling 3D printed scaffolds. Indeed, when comparing idealized to actual printed models (Figure 4 and 5), we have shown that the idealized model, in which layer fusion was not accounted for, was not able to provide accurate predictions because the geometry of the scaffold itself (e.g. scaffold height) was inaccurate. The actual printed models described filament diameter and amount of layer fusion as measured post-fabrication. For both *Aligned 1* and *Aligned 2* designs, modelling the idealized structures lead to a significant underestimation of the mechanical properties compared to the experimental results. On the other hand, the predicted compressive stiffness of the actual printed designs showed good agreement with the experiments, especially when the plasticity of PCL was also considered. Implementing an elastoplastic material model not only accurately predicted the compressive elastic modulus of the 3D printed constructs but also captured the mechanical behaviour past the yield point. This was observed for *Aligned 1*, *Aligned 2* and *Aligned 3* scaffold models.

To demonstrate how the proposed computational approach could be used to help inform the design of a scaffold prior to printing, the laydown filament pattern of the actual printed *Aligned 3* structure was theoretically modified to obtain *Single Offset* and *Double Offset* architectures. Introducing offset layers in one plane only (*Single Offset*) or in two planes (*Double Offset*) reduced the compressive stiffness by almost one order of magnitude (compressive modulus was decreased from 1.88 to 0.56 and ultimately to 0.22 MPa for *Aligned 3*, *Single Offset* and *Double Offset* designs, respectively), despite the scaffold porosity being maintained constant. Varying the filament pattern also reduced the permanent deformation within the scaffolds following the application of a defined level of compressive strain. In the stiffer *Aligned* scaffolds, deformation of the entire scaffold

primary occurs due to the filaments undergoing compressive strain. The scaffold is better designed to resist compressive deformation as columns of material are generated where filament layers overlap, and large strains and stresses are generated locally in the scaffold material at these points of overlap (Figure 4 and 6a, d). These large local stresses cause the material to locally undergo plastic deformation. In the softer *Offset* scaffolds, deformation of the scaffold occurs due to bending of the filaments. As the scaffold deforms in this way, it offers less resistance to compressive loading and smaller stresses and strains are generated locally within the scaffold material (Figure 7a, b); such smaller local stresses result in lower levels of permanent deformation. Experimental compression tests confirmed the ability of the FE modelling framework to produce scaffolds with specific mechanical attributes prior to their fabrication. Experimentally, the porosity of the analysed structures was the same and the compressive moduli matched the predicted values. In summary, we have developed a computationally efficient modelling approach using CAD-based scaffold representations that account for key geometrical features of the actual printed construct to predict the mechanical behaviour of 3D printed scaffolds. Employing such CAD-based FE models by using the average values of the scaffold geometrical parameters measured experimentally is advantageous as there is no need to develop computationally expensive sample-specific models that require complex and time-consuming imaging techniques (i.e. micro-CT) to accurately determine the geometry of the scaffolds. This approach is particularly beneficial in the initial scaffold design phase, although considering sample-specific geometries (which we have not undertaken in this study) will be important if trying to understand the variability in scaffold mechanical properties from print to print.

5 Conclusion

This study demonstrates the benefits of combining computational and experimental strategies for engineering spatially complex scaffolds. Specifically, a simple and relatively accessible FE strategy was developed, which was shown capable of successfully predicting the mechanical properties of 3D printed scaffolds prior to their fabrication. The geometric discrepancies between scaffold designs pre- and post-fabrication was found to be critical in developing FE models capable of accurately predicting the mechanical behaviour of 3D printed scaffolds. A number of strategies to modulate the structural and mechanical properties of 3D printed PCL scaffolds was explored, allowing constructs to be obtained with compressive properties spanning from the kPa to the MPa range. Thus, the proposed FEA method combined with 3D printing represents a powerful approach to producing biomaterial scaffolds mimicking the mechanical properties of a broad range of biological tissues.

Funding

This work was supported by the European Research Council (JointPrint; ERC-CoG-2014-647004).

Disclosure statement

No potential conflict of interest was reported by the authors

References

1. Brien, F. J. O. Biomaterials and scaffolds for tissue engineering. *Mater. Today* **14**, (2011).
2. Hollister, S. J. Porous scaffold design for tissue engineering. *Nat. Mater.* **4**, 518–

24 (2005).

3. Lohfeld, S., Cahill, S., Doyle, H. & McHugh, P. E. Improving the finite element model accuracy of tissue engineering scaffolds produced by selective laser sintering. *J. Mater. Sci. Mater. Med.* **26**, 1–12 (2015).

4. Park, J. S. *et al.* The effect of matrix stiffness on the differentiation of mesenchymal stem cells in response to TGF-β. *Biomaterials* **32**, 3921–30 (2011).

5. Murphy, S. V. & Atala, A. 3D bioprinting of tissues and organs. *Nat. Biotechnol.* **32**, 773–785 (2014).

6. Giannitelli, S. M., Accoto, D., Trombetta, M. & Rainer, A. Current trends in the design of scaffolds for computer-aided tissue engineering. *Acta Biomater.* **10**, 580–594 (2014).

7. Sachlos, E., Czernuszka, J. T., Gogolewski, S. & Dalby, M. Making tissue engineering scaffolds work. Review on the application ofsolid freeform fabrication technology to the production of tissue engineeringscaffolds. *Eur. Cells Mater.* **5**, 29–40 (2003).

8. Zein, I., Hutmacher, D. W., Tan, K. C. & Teoh, S. H. Fused deposition modeling of novel scaffold architectures for tissue engineering applications. *Biomaterials* **23**, 1169–1185 (2002).

9. Olubamiji, A. D. *et al.* Modulating mechanical behaviour of 3D-printed cartilage-mimetic PCL scaffolds: influence of molecular weight and pore geometry. *Biofabrication* **8**, 025020 (2016).

10. Woodfield, T. B. F. *et al.* Design of porous scaffolds for cartilage tissue engineering using a three-dimensional fiber-deposition technique. *Biomaterials* **25**, 4149–4161 (2004).

11. Roohani-Esfahani, S.-I., Newman, P. & Zreiqat, H. Design and Fabrication of 3D

printed Scaffolds with a Mechanical Strength Comparable to Cortical Bone to Repair Large Bone Defects. *Sci. Rep.* **6**, 19468 (2016).

12. Lacroix, D., Planell, J. A. & Prendergast, P. J. Computer-aided design and finite-element modelling of biomaterial scaffolds for bone tissue engineering. *Philos. Trans. R. Soc. A Math. Phys. Eng. Sci.* **367**, 1993–2009 (2009).

13. O'Reilly, A. & Kelly, D. J. Unravelling the Role of Mechanical Stimuli in Regulating Cell Fate During Osteochondral Defect Repair. *Ann. Biomed. Eng.* **44**, 3446–3459 (2016).

14. Woo Jung, J. *et al.* Evaluation of the effective diffusivity of a freeform fabricated scaffold using computational simulation. *J. Biomech. Eng.* **135**, 84501 (2013).

15. Eshraghi, S. & Das, S. Micromechanical finite-element modeling and experimental characterization of the compressive mechanical properties of polycaprolactone-hydroxyapatite composite scaffolds prepared by selective laser sintering for bone tissue engineering. *Acta Biomater.* **8**, 3138–3143 (2012).

16. Almeida, H. A. & Bártolo, P. J. Numerical simulations of bioextruded polymer scaffolds for tissue engineering applications. *Polym. Int.* **62**, 1544–1552 (2013).

17. Yan, K. C., Nair, K. & Sun, W. Three dimensional multi-scale modelling and analysis of cell damage in cell-encapsulated alginate constructs. *J. Biomech.* **43**, 1031–8 (2010).

18. Sun, W., Starly, B., Darling, A. & Gomez, C. Computer-aided tissue engineering: application to biomimetic modelling and design of tissue scaffolds. *Biotechnol. Appl. Biochem.* **39**, 49–58 (2004).

19. Lohfeld, S., Cahill, S., Doyle, H. & McHugh, P. E. Improving the finite element model accuracy of tissue engineering scaffolds produced by selective laser sintering. *J. Mater. Sci. Mater. Med.* **26**, 5376 (2015).

20. Campos Marin, A. & Lacroix, D. The inter-sample structural variability of regular tissue-engineered scaffolds significantly affects the micromechanical local cell environment. *Interface Focus* **5**, 20140097–20140097 (2015).

21. Gleadall, A., Ashcroft, I. & Segal, J. VOLCO: A predictive model for 3D printed microarchitecture. *Addit. Manuf.* **21**, 605–618 (2018).

22. Naghieh, S. *et al.* Modeling of the Mechanical Behavior of 3D Bioplotted Scaffolds Considering the Penetration in Interlocked Strands. *Appl. Sci.* **8**, 1422 (2018).

23. Rosa, D. S. *et al.* Evaluation of the Thermal and Mechanical Properties of and Their Blends. *J. Appl. Polym. Sci.* **91**, 3909–3914 (2004).

24. Ragaert, K. & Cardon, L. Bulk mechanical properties of thermoplastic poly-ε-caprolactone. *J. Mater. Sci. Mater. Med.* **20**, 1255–62 (2009).

25. Ribeiro, J. F. M. *et al.* Structural monitoring and modeling of the mechanical deformation of three-dimensional printed poly(ε-caprolactone) scaffolds. *Biofabrication* **9**, 025015 (2017).

26. Entezari, A. *et al.* Yielding behaviors of polymeric scaffolds with implications to tissue engineering. *Mater. Lett.* **184**, 108–111 (2016).

27. Boschetti, F., Pennati, G., Gervaso, F., Peretti, G. M. & Dubini, G. Biomechanical properties of human articular cartilage under compressive loads. *Biorheology* **41**, 159–166 (2004).

28. Athanasiou, K. A., Agarwal, A. & Dzida, F. J. Comparative study of the intrinsic mechanical properties of the human acetabular and femoral head cartilage. *J. Orthop. Res.* **12**, 340–349 (1994).

29. Salerno, A., Oliviero, M., Di Maio, E., Iannace, S. & Netti, P. A. Design of porous polymeric scaffolds by gas foaming of heterogeneous blends. *J. Mater.*

Sci. Mater. Med. **20**, 2043–2051 (2009).

30. Bracaglia, L. G. *et al.* 3D printing for the design and fabrication of polymer-based gradient scaffolds. *Acta Biomater.* **56**, 3–13 (2017).

31. Critchley, S. E. & Kelly, D. J. Bioinks for bioprinting functional meniscus and articular cartilage. *J. 3D Print. Med.* **1**, 269–290 (2017).

32. Daly, A. C. *et al.* 3D Bioprinting of Developmentally Inspired Templates for Whole Bone Organ Engineering. *Adv. Healthc. Mater.* **5**, 2353–62 (2016).

33. Liao, I.-C., Moutos, F. T., Estes, B. T., Zhao, X. & Guilak, F. Composite Three-Dimensional Woven Scaffolds with Interpenetrating Network Hydrogels to Create Functional Synthetic Articular Cartilage. *Adv. Funct. Mater.* **23**, 5833–5839 (2013).

34. Castilho, M. *et al.* Mechanical behavior of a soft hydrogel reinforced with three-dimensional printed microfibre scaffolds. *Sci. Rep.* **8**, 1245 (2018).

35. Bas, O. *et al.* Biofabricated soft network composites for cartilage tissue engineering. *Biofabrication* **9**, (2017).

36. Milan, J. L., Planell, J. A. & Lacroix, D. Computational modelling of the mechanical environment of osteogenesis within a polylactic acid-calcium phosphate glass scaffold. *Biomaterials* **30**, 4219–4226 (2009).

37. Hendrikson, W. J., van Blitterswijk, C. A., Rouwkema, J. & Moroni, L. The Use of Finite Element Analyses to Design and Fabricate Three-Dimensional Scaffolds for Skeletal Tissue Engineering. *Front. Bioeng. Biotechnol.* **5**, 1–13 (2017).

38. Moroni, L. *et al.* Finite Element Analysis of Meniscal Anatomical 3D Scaffolds: Implications for Tissue Engineering. *Open Biomed. Eng. J.* **1**, 23–34 (2007).

39. Bas, O. *et al.* An Integrated Design, Material, and Fabrication Platform for Engineering Biomechanically and Biologically Functional Soft Tissues. *ACS*

Appl. Mater. Interfaces **9**, 29430–29437 (2017).

40. Cahill, S., Lohfeld, S. & McHugh, P. E. Finite element predictions compared to experimental results for the effective modulus of bone tissue engineering scaffolds fabricated by selective laser sintering. *J. Mater. Sci. Mater. Med.* **20**, 1255–1262 (2009).

41. Doyle, H., Lohfeld, S., McDonnell, P. & McHugh, P. Evaluation of a Multiscale Modelling Methodology to Predict the Mechanical Properties of PCL/β-TCP Sintered Scaffold Materials. *Ann. Biomed. Eng.* **43**, 1989–1998 (2014).

42. Daly, A. C. *et al.* 3D Bioprinting for Cartilage and Osteochondral Tissue Engineering. *Adv. Healthc. Mater.* **1700298**, 1700298 (2017).

43. Woodruff, M. A. & Hutmacher, D. W. The return of a forgotten polymer - Polycaprolactone in the 21st century. *Prog. Polym. Sci.* **35**, 1217–1256 (2010).

44. Tellis, B. C. *et al.* Trabecular scaffolds created using micro CT guided fused deposition modeling. *Mater. Sci. Eng. C* **28**, 171–178 (2008).

45. Domingos, M. *et al.* Effect of process parameters on the morphological and mechanical properties of 3D Bioextruded poly(1-caprolactone) scaffolds. *Rapid Prototyp. J.* **18**, 56–67 (2012).

46. Naghieh, S., Karamooz Ravari, M. R., Badrossamay, M., Foroozmehr, E. & Kadkhodaei, M. Numerical investigation of the mechanical properties of the additive manufactured bone scaffolds fabricated by FDM: The effect of layer penetration and post-heating. *J. Mech. Behav. Biomed. Mater.* **59**, 241–250 (2016).

47. Campoli, G. *et al.* Mechanical properties of open-cell metallic biomaterials manufactured using additive manufacturing. *Mater. Des.* **49**, 957–965 (2013).

48. Melancon, D. *et al.* Mechanical characterization of structurally porous

biomaterials built via additive manufacturing: experiments, predictive models, and design maps for load-bearing bone replacement implants. *Acta Biomater.* **63**, 350–368 (2017).

49. Karamooz Ravari, M. R., Kadkhodaei, M., Badrossamay, M. & Rezaei, R. Numerical investigation on mechanical properties of cellular lattice structures fabricated by fused deposition modeling. *Int. J. Mech. Sci.* **88**, 154–161 (2014).

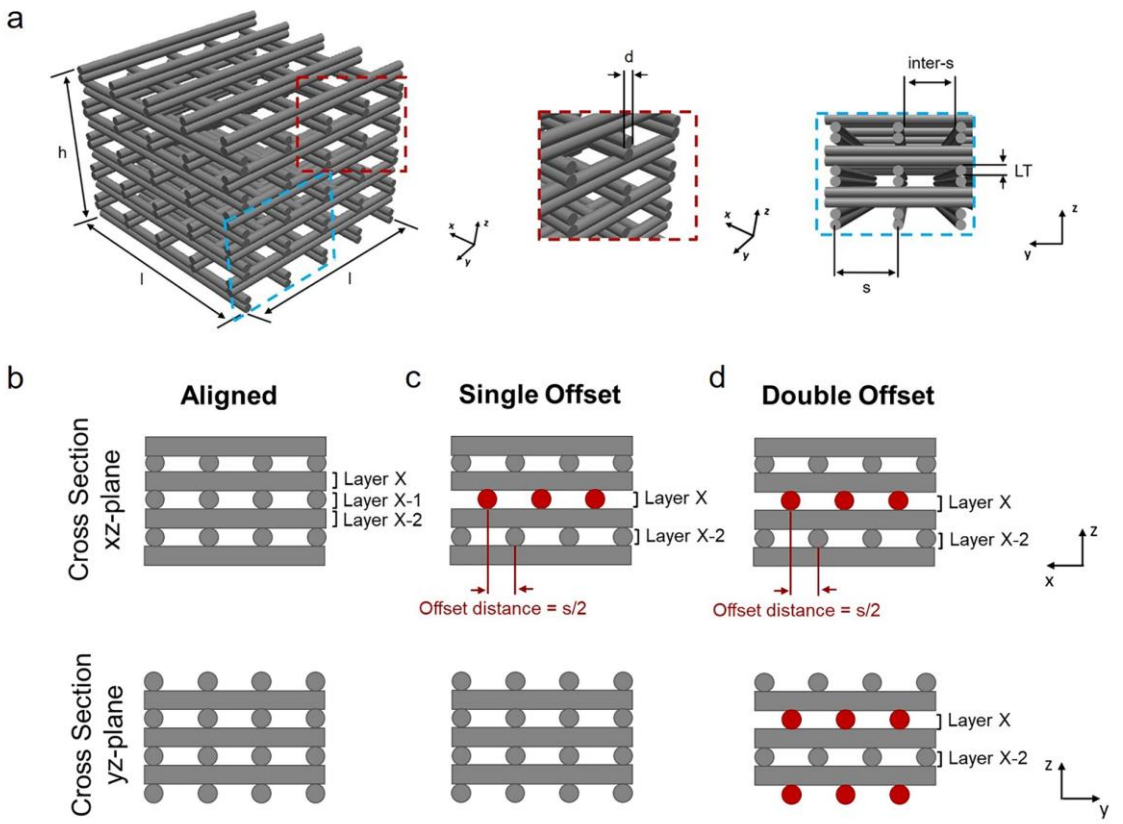

Figure 1. (a) Scaffold geometrical features: d, fibre diameter; s, fibre spacing; inter-s, fibre inter-spacing; LT, layer thickness; l, length of the scaffold; h, height of the scaffold. (b-d) Schematic describing the different filament patterns of the designed scaffolds consisting of a regular orthogonal architecture in the case of (b) the Aligned pattern, whereas offset layers are present only in one plane for (c) the *Single Offset* pattern or in both planes for (d) the *Double Offset* pattern. Offset layers are indicated in red.

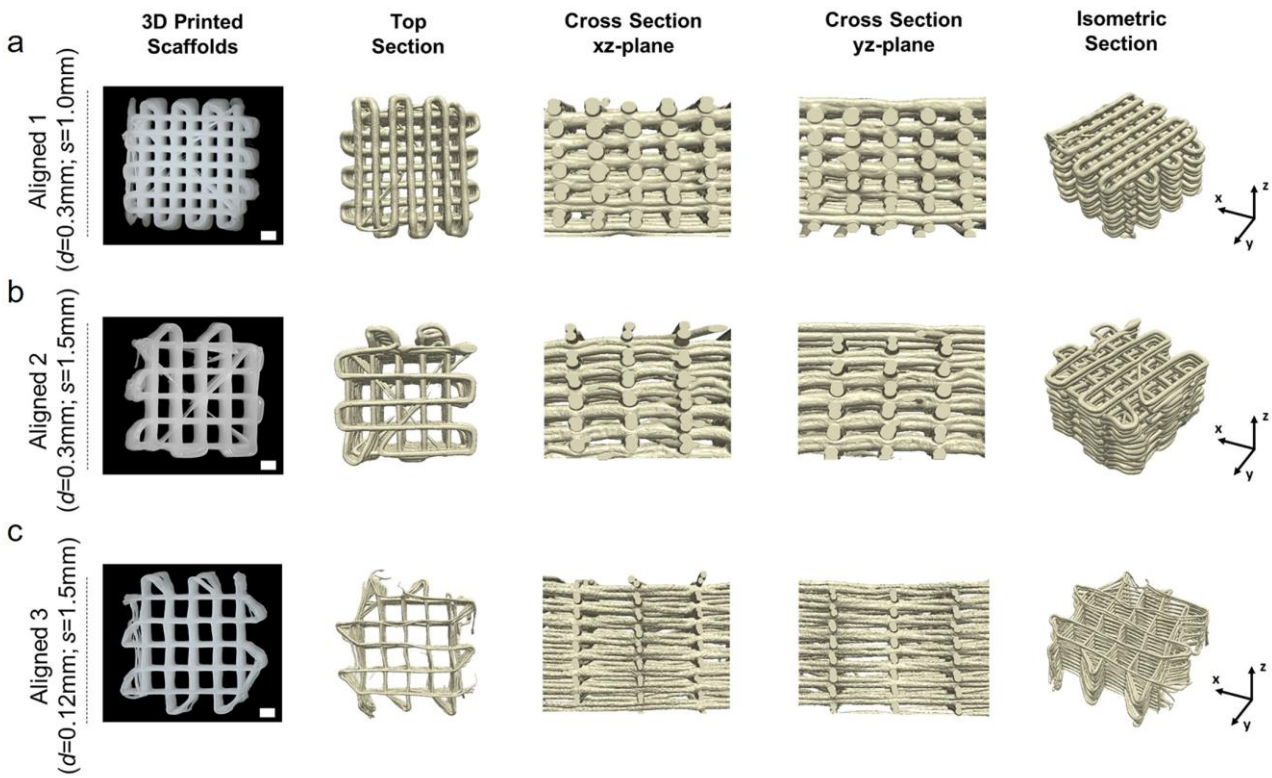

682

683 **Figure 2.** Microscopy and micro-CT images of (a) *Aligned 1* (*d*=0.3mm; *s*=1.0mm), (b)

684 *Aligned 2* (*d*=0.3mm; *s*=1.5mm) and (c) *Aligned 3* (*d*=0.12mm; *s*=1.5mm) scaffolds

685 fabricated via 3D printing. Scale bar: 1 mm.

686

687

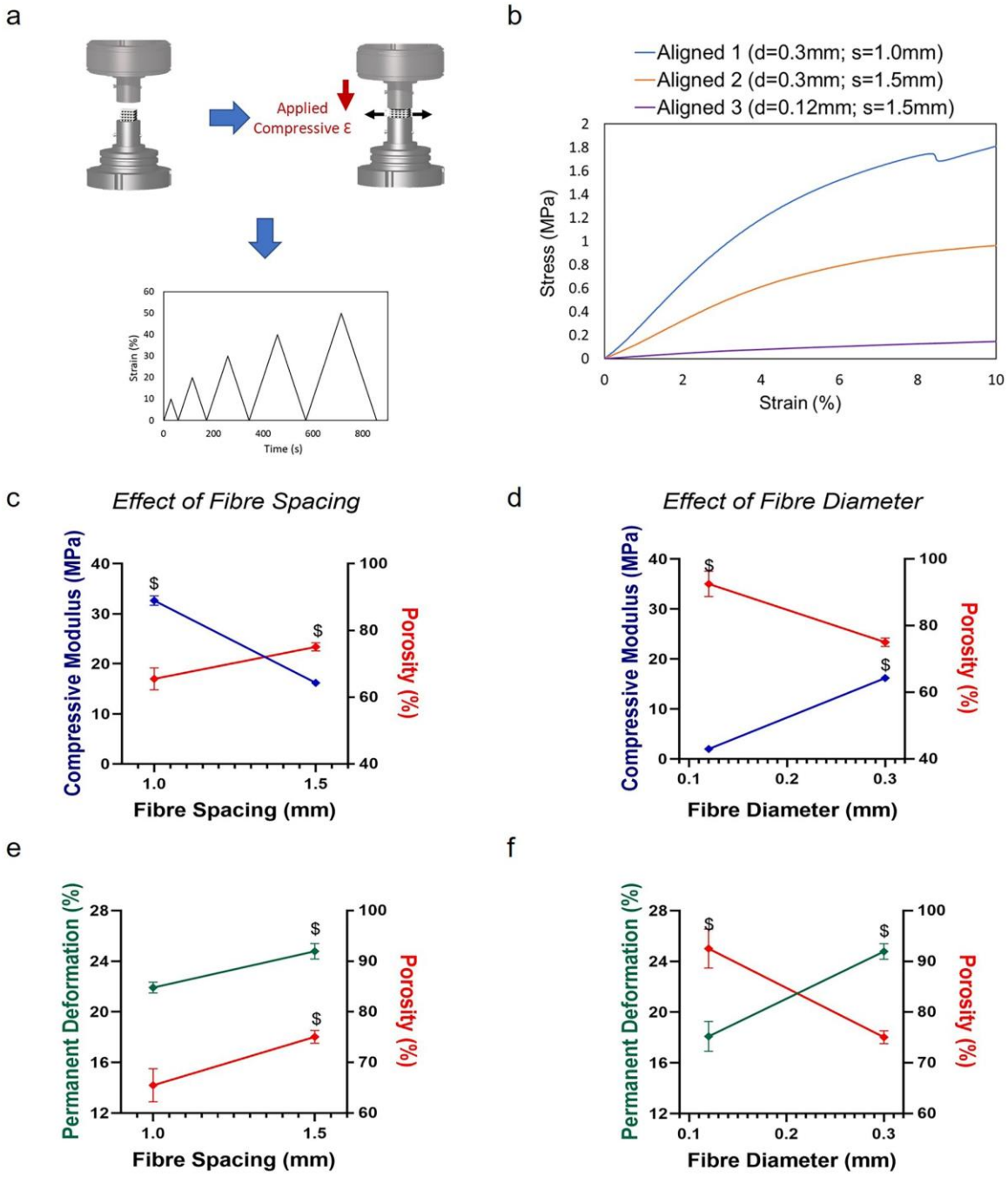

Figure 3. (a) Schematic illustration of the mechanical testing set-up and protocol used to perform unconfined cyclic compression tests. (b) Representative stress-strain curves for *Aligned 1* (*d*=0.3mm; *s*=1.0mm), *Aligned 2* (*d*=0.3mm; *s*=1.5mm) and *Aligned 3* (*d*=0.12mm; *s*=1.5mm) architectures. Effect of modifying (c,e) fibre spacing and (d,f) fibre diameter on porosity, compressive modulus and permanent deformation of 3D-printed PCL constructs. $^{\$}p<0.01$, n = 4 per group.

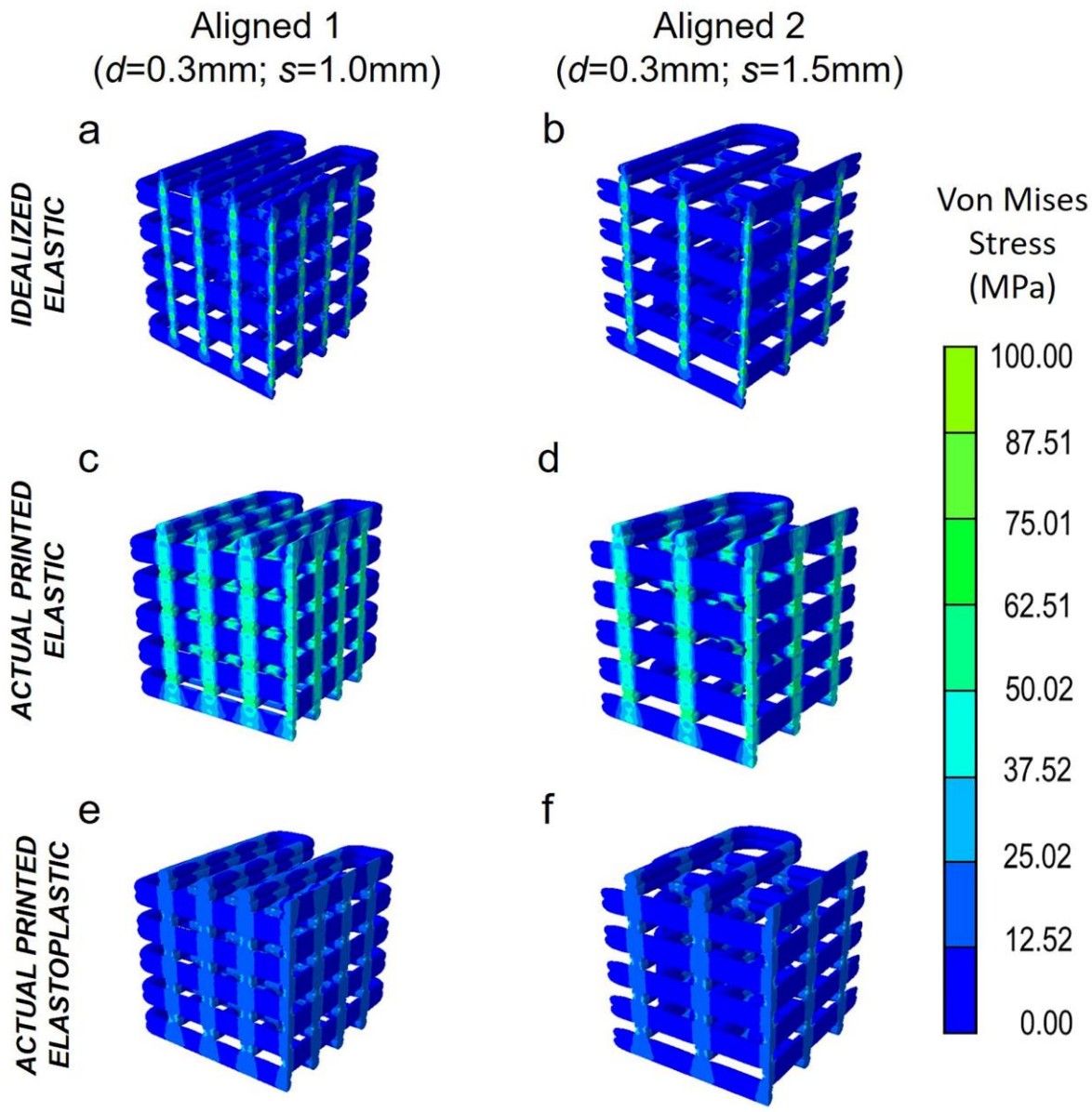

695

696 **Figure 4.** Comparison of von Mises stress distribution in (a,b) idealized elastic, (c,d)

697 actual printed elastic and (e,f) actual printed elastoplastic models for (a,c,e) *Aligned 1*

698 (*d*=0.3mm; *s*=1.0mm) and (b,d,f) *Aligned 2* (*d*=0.3mm; *s*=1.5mm) designs.

699

700

701

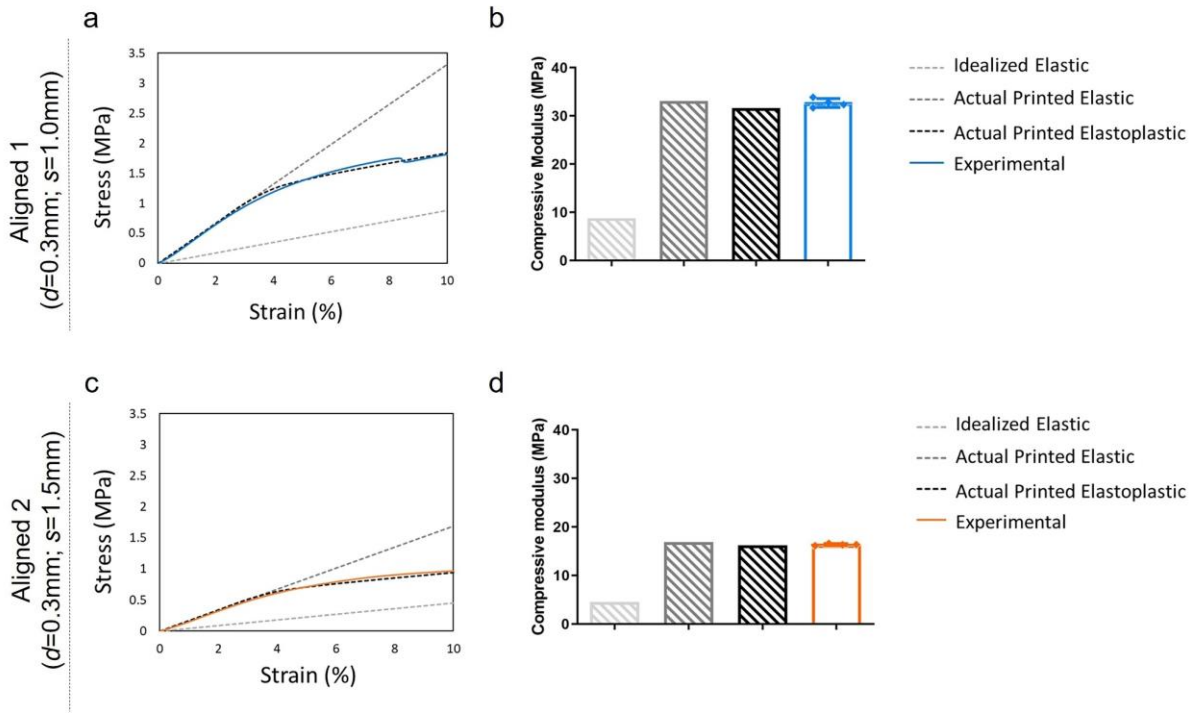

Figure 5. (a-d) Predicted (idealized elastic, actual printed elastic and actual printed elastoplastic) and experimental compression properties for *Aligned 1* (*d*=0.3mm; *s*=1.0mm) and *Aligned 2* (*d*=0.3mm; *s*=1.5mm) designs. Compression stress-strain diagrams (a,c) and compressive modulus values (b,d) for (a,b) *Aligned 1*(*d*=0.3mm; *s*=1.0mm) and (c,d) *Aligned 2* (*d*=0.3mm; *s*=1.5mm) structures.

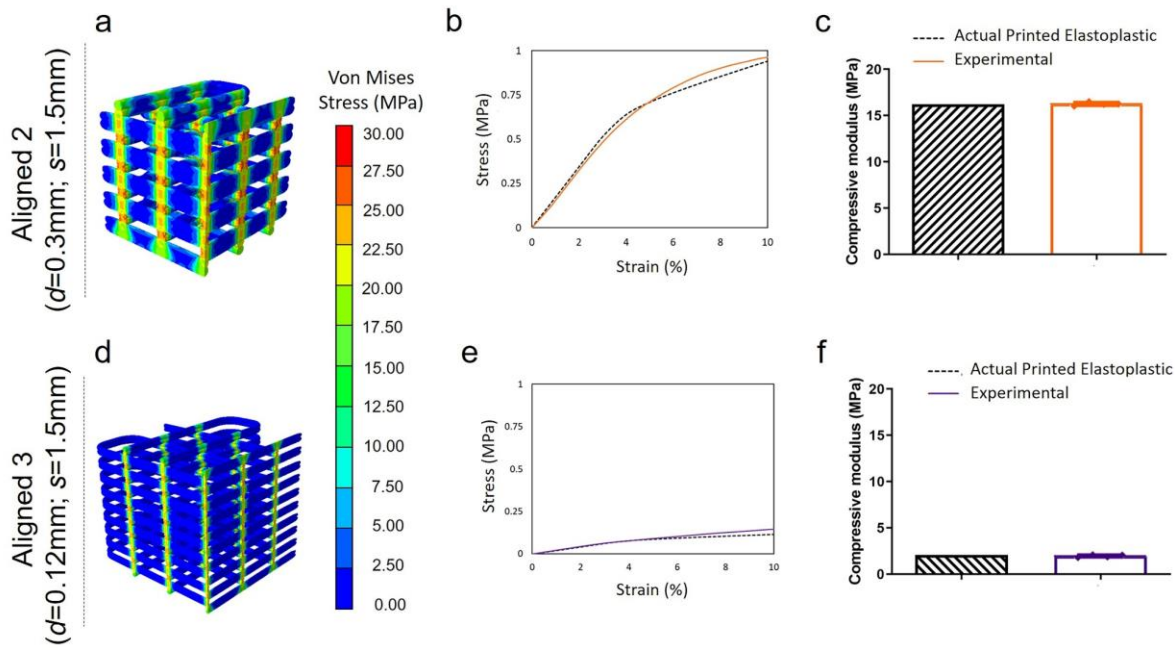

718

719 **Figure 6.** Comparison of von Mises stress distribution in actual printed elastoplastic
720 models for (a) *Aligned 2* (*d*=0.3mm; *s*=1.5mm) and (d) *Aligned 3* (*d*=0.12mm; *s*=1.5mm)
721 designs. Predicted and experimental (b,e) compression stress-strain diagrams and (c,f)
722 compressive moduli for (b,c) *Aligned 2* (*d*=0.3mm; *s*=1.5mm) and (e,f) *Aligned 3*
723 (*d*=0.12mm; *s*=1.5mm) structures.

724

725

726

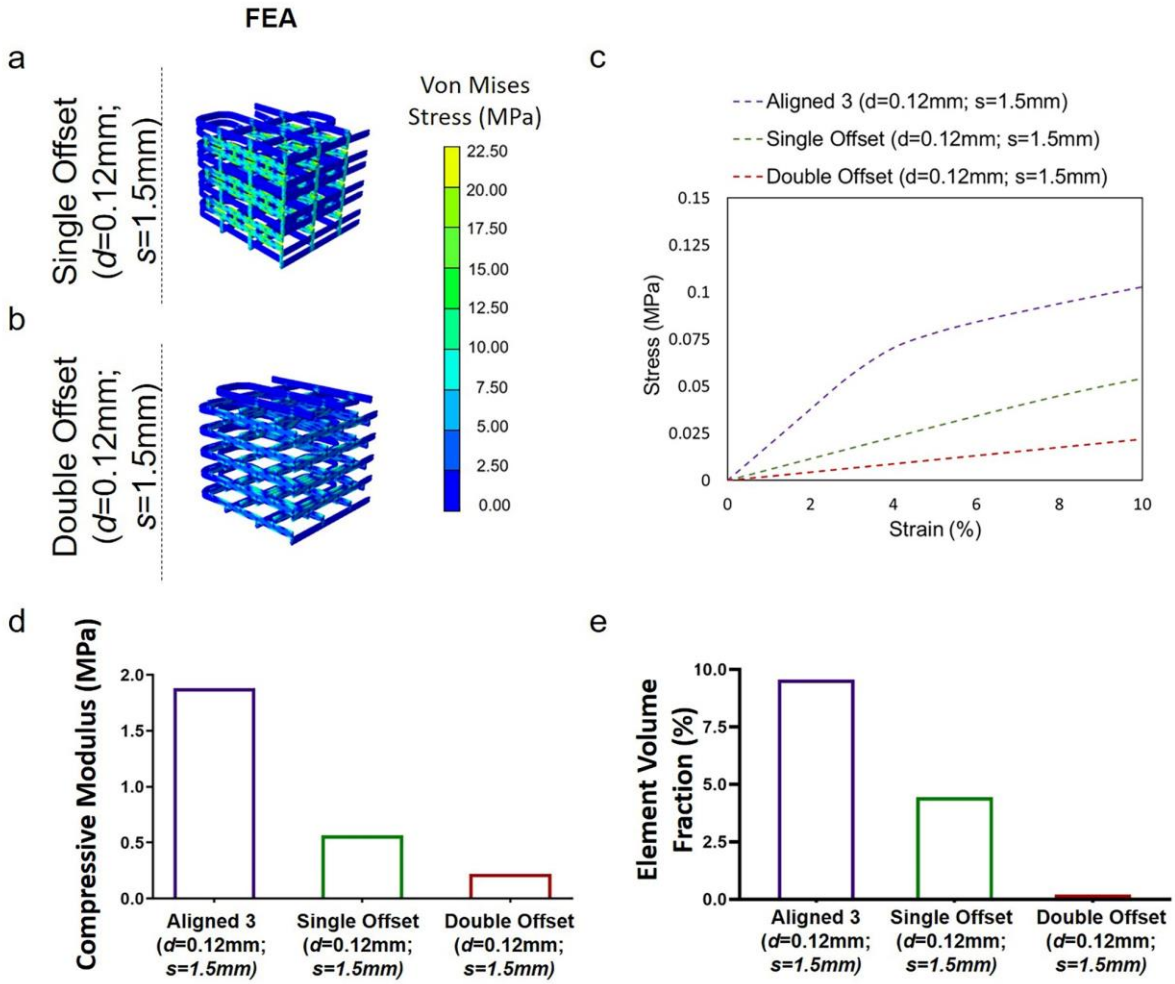

Figure 7. Von Mises stress contour plots for (a) *Single Offset* (*d*=0.12mm; *s*=1.5mm) and (b) *Double Offset* (*d*=0.12mm; *s*=1.5mm) structures. Computational (c) compression stress-strain graph, (d) compressive moduli and (e) element volume fraction experiencing stresses greater than 17 MPa (PCL yield stress) comparing *Aligned 3* (*d*=0.12mm; *s*=1.5mm), *Single Offset* (*d*=0.12mm; *s*=1.5mm) and *Double Offset* (*d*=0.12mm; *s*=1.5mm) geometries.

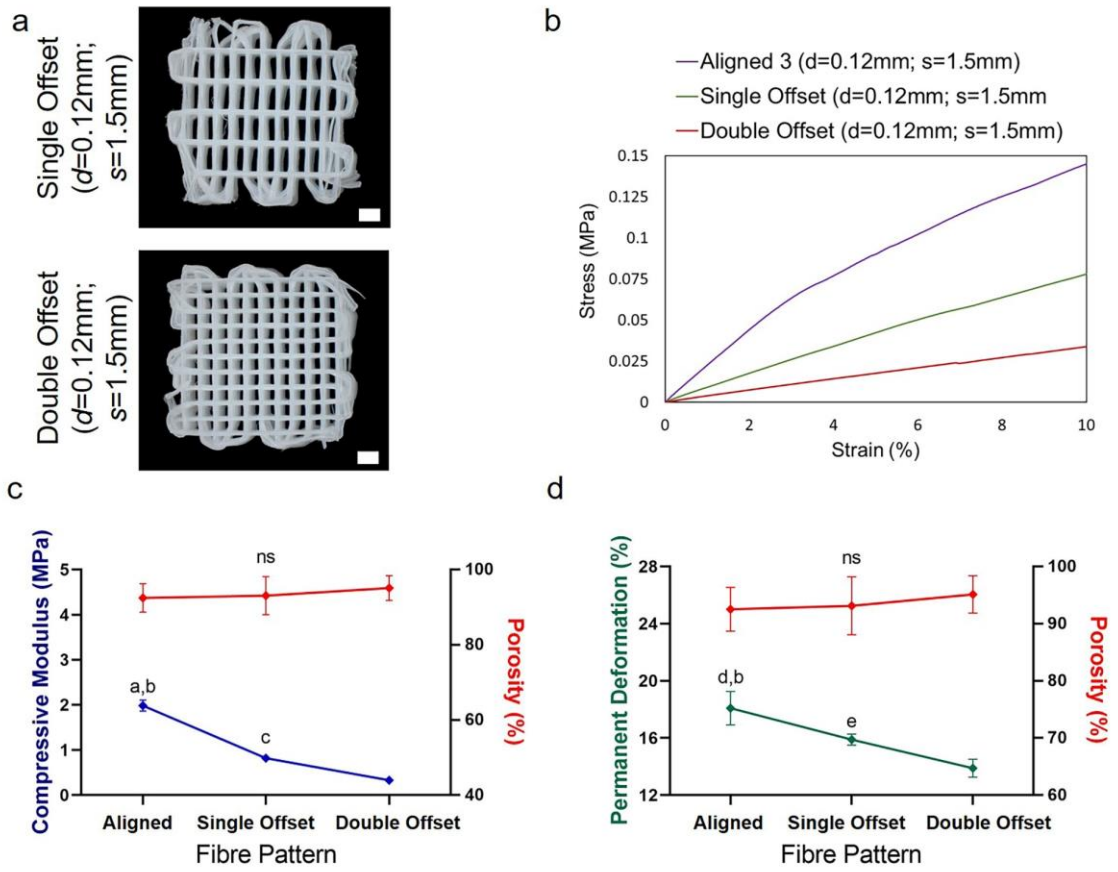

736

737 **Figure 8.** (a) Microscopy images of *Single Offset* (*d*=0.12mm; *s*=1.5mm) (top) and *Double*
738 *Offset* (*d*=0.12mm; *s*=1.5mm) (bottom) 3D-printed PCL scaffolds; scale bar: 1mm.
739 Representative experimental stress-strain curves for *Aligned 3* (*d*=0.12mm; *s*=1.5mm),
740 *Single Offset* (*d*=0.12mm; *s*=1.5mm) and *Double Offset* (*d*=0.12mm; *s*=1.5mm) architectures.
741 (c,d) Effect of modifying fibre pattern on porosity, compressive modulus and permanent
742 deformation of 3D-printed PCL constructs. [a]p<0.0001 *Aligned 3* (*d*=0.12mm; *s*=1.5mm) vs.
743 *Single Offset* (*d*=0.12mm; *s*=1.5mm), [b]p<0.0001 *Aligned 3* (*d*=0.12mm; *s*=1.5mm) vs.
744 *Double Offset* (*d*=0.12mm; *s*=1.5mm), [c]p<0.0001 *Single Offset* (*d*=0.12mm; *s*=1.5mm) vs.
745 *Double Offset* (*d*=0.12mm; *s*=1.5mm) when evaluating the compressive moduli, n = 4 per
746 group. [d]p<0.01 *Aligned 3* (*d*=0.12mm; *s*=1.5mm) vs. *Single Offset* (*d*=0.12mm; *s*=1.5mm),
747 [b]p<0.0001 *Aligned 3* (*d*=0.12mm; *s*=1.5mm) vs. *Double Offset* (*d*=0.12mm; *s*=1.5mm),
748 [e]p<0.01 *Single Offset* (*d*=0.12mm; *s*=1.5mm) vs. *Double Offset* (*d*=0.12mm; *s*=1.5mm) when
749 evaluating the permanent deformation, n = 4 per group.

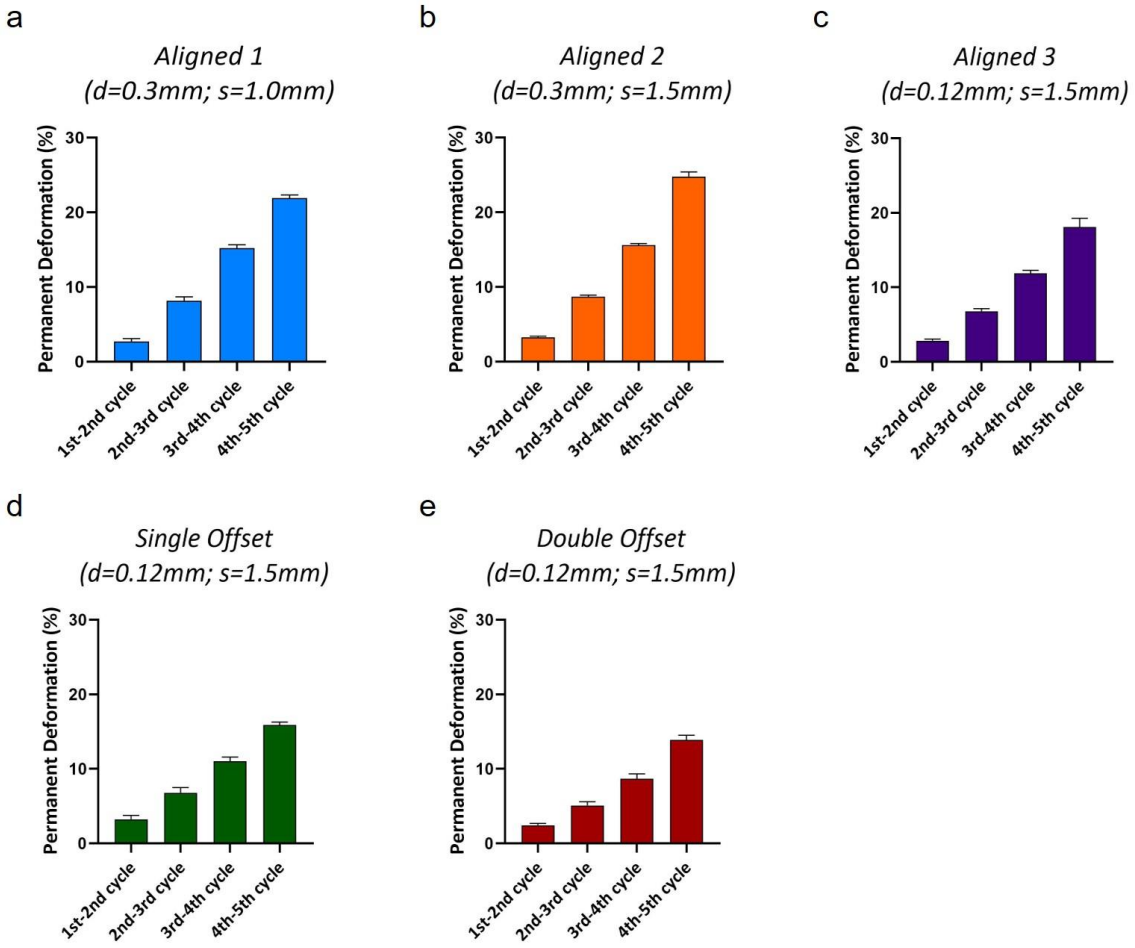

Supplementary Figure 1. Permanent deformation at each applied compressive strain amplitude for (a) *Aligned 1* (*d*=0.3mm; *s*=1.0mm), (b) *Aligned 2* (*d*=0.3mm; *s*=1.5mm), (c) *Aligned 3* (*d*=0.12mm; *s*=1.5mm), (d) *Single Offset* (*d*=0.12mm; *s*=1.5mm) and (e) *Double Offset* (*d*=0.12mm; *s*=1.5mm) scaffold geometries.

762 **Table 1.** Summary of FDM printing parameters.

Printing Parameters	***Aligned 1*** **(*d*=0.3mm; *s*=1.0mm)** ***Aligned 2*** **(*d*=0.3mm; *s*=1.5mm)**	***Aligned 3*** **(*d*=0.12mm; *s*=1.5mm)** ***Single Offset*** **(*d*=0.12mm; *s*=1.5mm)** ***Double Offset*** **(*d*=0.12mm; *s*=1.5mm)**
Needle (Gauge)	25	30
Layer Thickness (mm)	0.22	0.1
Pressure (MPa)	0.5	0.1
Printing Speed (mm/s)	4	6
Extrusion Speed (revs/m)	14	10
Tank Temperature (°C)	70	86
Needle Temperature (°C)	70	78

763

764 **Table 2.** Idealized geometrical parameters defined for scaffold fabrication versus actual printed geometrical parameters measured after

765 fabrication.

766

	Fibre Diameter (mm)		**Fibre Spacing (mm)**		**Fibre Inter-spacing (mm)**		**Layer Fusion (mm)**		**Porosity (%)**	
	Idealized Geometry	Actual Printed Geometry	Idealized Geometry	Actual Printed Geometry	Idealized Geometry	Actual Printed Geometry	Idealized Geometry	Actual Printed Geometry	Idealized Geometry	Actual Printed Geometry
Aligned 1 **(*d*=0.3mm; *s*=1.0mm)**	0.26	0.307 ± 0.014	1	1.064 ± 0.106	0.74	0.660 ± 0.017	0	0.084 ± 0.011	80.4	67.48 ± 0.931
Aligned 2 **(*d*=0.3mm; *s*=1.5mm)**	0.26	0.296 ± 0.021	1.5	1.465 ± 0.114	1.24	1.168 ± 0.089	0	0.076 ± 0.012	86.2	75.05 ± 1.267
Aligned 3 **(*d*=0.12mm; *s*=1.5mm)**	0.16	0.121 ± 0.015	1.5	1.540 ± 0.061	1.34	1.373 ± 0.025	0	0.018 ± 0.009	91.9	92.50 ± 3.840
Single Offset **(*d*=0.12mm; *s*=1.5mm)**	0.16	0.127 ± 0.030	1.5	1.526 ± 0.035	1.34	1.392 ± 0.041	0	0.022 ± 0.012	92.1	93.10 ± 5.081
Double Offset **(*d*=0.12mm; *s*=1.5mm)**	0.16	0.130 ± 0.023	1.5	1.530 ± 0.092	1.34	1.379 ± 0.103	0	0.025 ± 0.003	92.8	95.13 ± 3.290

767

768 **Table 3.** Elastic and plastic material parameters used for the numerical analysis of PCL
769 scaffolds where E is the Young's modulus; ν is the Poisson's ration; σ_{true}^{y} is the true
770 yield stress; ε_{pl}^{y} is the true plastic yield strain; σ_{true}^{f} is the true stress at failure; ε_{pl}^{f} is the
771 true plastic strain at failure.

Material	Material model	Material Properties
PCL	Isotropic elastic	$E = 430\ MPa$ $\nu = 0.3$
	Isotropic plastic	$\sigma_{true}^{y} = 17.745\ MPa$ $\varepsilon_{pl}^{y} = 0$ $\sigma_{true}^{f} = 113.39\ MPa$ $\varepsilon_{pl}^{f} = 1.3316$

772